Article

Biosynthesis, Physicochemical and Magnetic Properties of Inverse Spinel Nickel Ferrite System

Ghadah M. Al-Senani [1], **Foziah F. Al-Fawzan** [1], **Rasmiah S. Almufarij** [1], **Omar H. Abd-Elkader** [2,3,*]
and Nasrallah M. Deraz [4]

1   Department of Chemistry, College of Science, Princess Nourah bint Abdulrahman University,
    P.O. Box 84428, Riyadh 11671, Saudi Arabia
2   Physics and Astronomy Department, Science College, King Saud University,
    P.O. Box 2455, Riyadh 11451, Saudi Arabia
3   Electron Microscope and Thin Films Department, Physics Research Institute, National Research Centre,
    P.O. Box 21111, Giza 12622, Egypt
4   Physical Chemistry Department, National Research Centre, P.O. Box 21111, Giza 12622, Egypt
*   Correspondence: omabdelkader7@ksu.edu.sa

Abstract: Nanosized Ni ferrite has been prepared by an ecofriendly green synthesis approach based on the self-combustion method. In this route, the egg white as a green fuel was employed with two different amounts (3 and 10 mL). The XRD results display the formation of a stoichiometric $NiFe_2O_4$-type inverse spinel structure with a lattice parameter located at 0.8284 nm and 0.8322 nm. Additionally, the nickel ferrites' typical crystallite size, as synthesized, ranged between 4 and 18 nm. Indicating the development of ferrite material, FTIR analysis shows two distinctive vibrational modes around 600 cm^{-1} and 400 cm^{-1}. TEM measurements show the formation of nanosized particles with semispherical-type structure and some agglomerations. As the egg white concentration rises, the surface area, total pore volume, and mean pore radius of the material, as prepared, all decrease, and according to the surface area parameters discovered using BET analysis. Based on VSM analysis, the values of saturation magnetization are 6.6589 emu/g and 37.727 emu/g, whereas the coercivity are 159.15 G and 113.74 G. The as-synthesized Ni ferrites fit into the pseudo-single domain predicated by the squareness values (0.1526 and 0.1824). It is mentioned that increasing the egg white content would promote the magnetization of $NiFe_2O_4$.

Keywords: XRD; FTIR; HRTEM; $NiFe_2O_4$; squareness; magnetization

1. Introduction

Metal oxides have occupied a great place in scientific research, especially the transitional metal oxides. These oxides are divided between single and mixed oxides, with different physical and chemical properties for each of them. The separate oxides directly interact with one another, resulting in the formation of the mixed transition metal oxides, which have new and distinct features from the individual oxides. The solid-state reaction between these oxides was controlled by many factors, including the preparation method, calcination temperature, doping, and the nature and precursor of the transitional metals [1]. The mechanism of this reaction depends mainly on both the mobility of the reacted oxides and the contact surface area between them [2]. The solid-state reaction often leads to desirable and economically valuable materials, depending on their multiple uses in the many applied fields. Due to the requirement for this reaction to occur at a high temperature and over a timescale that may be quite lengthy, this interaction may encounter various problems that are considered defects, which must periodically be avoided. Therefore, overcoming these two disadvantages has been a major goal for many scientists, through careful selection of the preparation method. Accordingly, the method of preparation is the

key factor to obtain different useful products, such as ferrites, in the least time and with the least possible energy [3].

The great importance of ferrite-based materials is due to their multiple technological applications such as electronic devices, catalysis, sensors, memory devices, data storage, and telecommunications [4–7]. An important role of these materials could be attributed to their interesting electrical, magnetic, and dielectric characteristics [8,9]. The preparation of ferrites in the form of nanoparticles (NPs) resulted in progressive modifications in their electronic technological applications and also opened the way for new and exciting research fields such as biotechnology and water treatment [10–12]. In fact, the ferrites in the nanoscale have additional characteristics compared with those in the bulk form, due to the high surface-to-volume ratio and their superparamagnetic properties [9,11].

In our previous studies, we dealt with the preparation of many ferrites, including doped, single, and mixed nickel ferrites [3,5,13–16]. Our preparations of different nickel ferrites ($NiFe_2O_4$) depend on the glycine-assisted combustion method. Indeed, this method resulted in the formation of $NiFe_2O_4$ nanoparticles. Effects of the doping by magnesia, the substitution by Co and Zn oxides, and changing the glycine content have been studied [5,13–15]. The magnetization of the as-prepared nickel ferrites was increased by increasing the glycine content and also with the substitution by Co and Zn oxides [5,13,15,16]. $NiFe_2O_4$ NPs showed good adsorption efficiency for sulfur from commercial kerosene, depending on their textural and chemical properties [13]. The magnetization of nickel ferrite, on the other hand, was reduced as a result of Mg doping [14]. In the spinel nickel ferrites, these effects were explored in terms of the cation distribution between the octahedral and tetrahedral sites [17].

Recently, there have been a lot of conventional techniques for the preparation of ferrite-based nanoparticles such as coprecipitation, sol–gel, microemulsion, citrate precursor, and sonochemical synthesis [18–21]. Unfortunately, there are still many limitations to these methods, which makes us resort to nontraditional methods such as the combustion method based on egg whites, due to its functions of emulsification, foaming, and gelling. The adsorption coagulation and solidification phenomenon will appear when the metal ions are mixed with egg white, yielding a gelled precursor. The creation of the required ferrite can frequently be achieved by heating this gelled precursor for a brief time at a relatively moderate temperature [22]. So, the egg-white-mediated combustion method is an economical, friendly, and simple method. So far, per the knowledge of the authors, none of the literature available on the synthesis of ferrite materials, using the egg white precursor technique, are without the heat treatment being above 500 °C for some hours [23–25]. The heat treatment of the gelled precursor in this study was performed at a temperature of less than 300 °C, for no longer than a quarter of an hour, which is the difference between the literature and this report, as it requires little time or energy.

In the present work, we report for fabrication of nanocrystalline $NiFe_2O_4$ at a relatively low temperature by an environmentally friendly and cost-effective route by using egg-white-precursor technique. However, alternative techniques were used to investigate the impact of the egg white content on the formation, structural, morphological, surface, and magnetic properties.

2. Materials and Methods

2.1. Materials

Nickel (II) nitrate hexahydrate and ferric nitrate hydrate, with linear formulas Ni $(NO_3)_2.6H_2O$ and Fe $(NO_3)_3. 9H_2O$, respectively, were used as chemical materials. Sigma-Aldrich Company (Darmstadt, Taufkirchen, Germany) provided these ingredients. These were quantitative reagents that were applied without further refining. The egg white was derived from raw eggs provided by nearby hens.

2.2. Preparation Route

Two samples (S1 and S2) of $NiFe_2O_4$ were prepared by using egg-white-mediated combustion method. The first sample (S1) was synthesized by good mixing of equimolar ratio of nickel nitrate hexahydrate and ferric nitrate hydrate with 3 mL egg white in a crucible, taking into account the stoichiometric ratio Fe/Ni = 2. For the purpose of evaporating water and increasing viscosity, the prepared liquid was initially agitated at 60 °C. Following that, a gel was produced by heating the solution to 120 °C. The resulting precursor gel was then calcined at 300 °C for 15 min to attain a crucible temperature. At this point, a lot of foam began to develop, and a spark appeared in one corner and quickly spread throughout the mass, producing the end product, which was a thick and fluffy solid. The second sample (S2) was prepared with the same procedures but in presence of 10 mL egg white.

2.3. Characterization Techniques

Utilizing a BRUKER D8 advance diffractometer, measurements of various mixed solids were made utilizing X-ray diffraction technology (Karlsruhe, Germany). The patterns were run using Cu Kα radiation at 40 kV and 40 mA with a $2°$ min^{-1} scanning speed. Based on X-ray diffraction line broadening and Scherrer equation calculations, the crystallite size of $NiFe_2O_4$ contained in the examined materials was determined [26].

$$d = \frac{B\lambda}{\beta \cos \theta} \tag{1}$$

where d is the average crystallite size of the phase being studied, B is the Scherrer constant (0.89), λ is the wavelength of the X-ray beam being employed, β is the full-width half maximum (FWHM) of diffraction, and θ is the Bragg's angle.

Perkin-Elmer Spectrophotometer (Unit a Llantrisant CF72 United Kingdom) was used to determine the Fourier-transform infrared spectrum (FTIR) of various materials (type 1430). The FTIR spectra were measured between 1000 and 400 cm^{-1}. Then, 200 mg of IR-grade K Br that has been vacuum-dried was combined with two milligrams of each solid sample. The combination was ground for 3 min in a vibratory ball mill, then put in a steel die that was 13 mm in diameter, and put under 12 tons of pressure to scatter it. The holder of the double-grating FTIR spectrophotometer was filled with the identical disks.

Using JEOL JAX-840A (Tokyo, Japan) and JEOL Model 1230 transmission electron microscopes (TEM) operated at 100 Kev, the specimens on particular solvent and by deep coating of carbon-filmed copper grid in the solution and leave the grid to evaporate the solvent for hours before analysis. Disperse the sample in an ultrasonically for a short period of time to disperse individual particles over the mount arrangement and copper grids.

Using a traditional volumetric equipment (Brunauer–Emmett–Teller method) and surface area analyzers from Micrometrics' Gemini VII 2390 V1.03 series, specific surface area (S_{BET}), total pore volume (V_P), and mean pore radius ($\hat{r}$) of diverse materials were calculated (Microtrac, Alpharetta, GA, USA). Before the measurements, each sample was out-gassed for 2 h at 200 °C and a lower pressure of 105 Torr. The magnetic characteristics of the analyzed solids were examined using a vibrating sample magnetometer (VSM; 9600-1 LDJ, USA) with a maximum applied field of 20 kG.

3. Results

3.1. XRD Measurements

By employing the XRD technique, it is possible to investigate how different crystalline phases with various structural properties emerge in nickel ferrites, as they are being created. The S1 and S2 specimens' X-ray diffract grams are illustrated in Figure 1. Analysis of this graph supports the following:
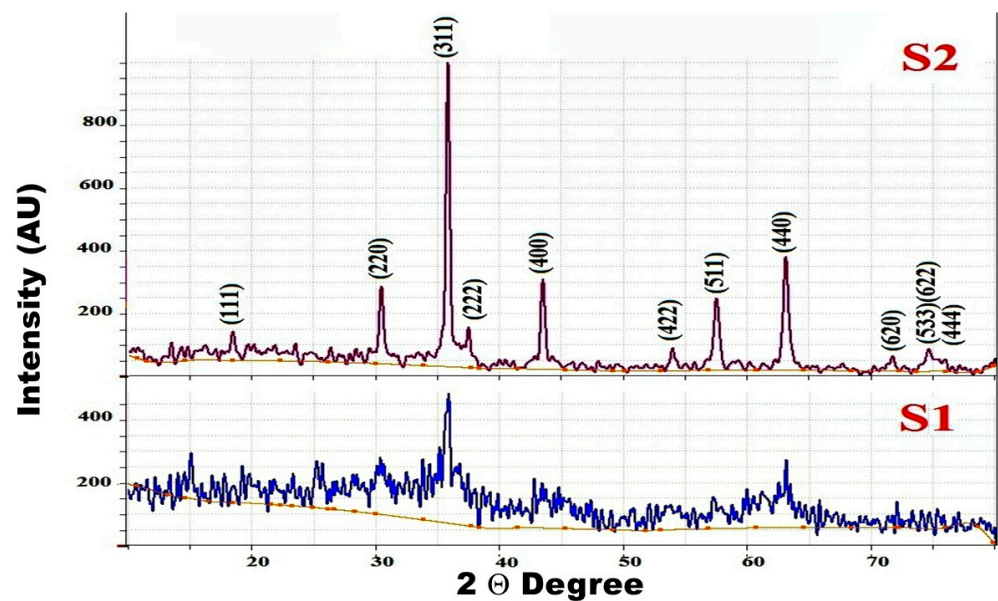
Figure 1. XRD patterns of S1 and S2 samples.

(i) The S1 and S2 samples have a crystalline nature because their XRD patterns consisted of various specified peaks. The reported data in PDF No. 44-1485 was matched with the XRD patterns of the S1 and S2 solids, confirming the formation of spinel $NiFe_2O_4$ crystallites. In other words, the indexing planes (111), (220), (311), (222), (400), (422), (511), (440), (620), (533), (522), and (444) of a cubic spinel structure with the Fd3m space group are associated with the diffraction peaks at 2θ = 18.60°, 31.20°, 30.62°, 35.78°, 37.66°, 43.67°, 54.10°, and 57.66°.

(ii) The peak height of the $NiFe_2O_4$ crystallites produced increased as the egg white content was increased. This conclusion does not indicate that there is no secondary phase in the S1 sample; instead, it indicates that the increase in egg white concentration has increased the solid–solid interactions of the secondary phases, leading to nickel ferrite. To further support the growth in the solid-state reaction between the reactive oxides to form Ni ferrite, there was a shift in the peak positions, as the egg white content increased. According to the XRD results, the S2 sample's complete conversion of the reactive oxides without the presence of a secondary phase confirms the phase purity of $NiFe_2O_4$ as the final product.

The structural examination of the as-prepared ferrite, based on the XRD results, allowed us to estimate a number of parameters, including the crystallite size (d), lattice constant (a), unit cell volume (V), X-ray density (D_x), distance between the magnetic ions (L_A and L_B), ionic radii (r_A, r_B), dislocation density (δ), and bond lengths (A-O and B-O) on the tetrahedral (A) sites and octahedral (B) sites. Increased egg white content led to higher values for the d, a, L_A, L_B, r_A, r_B, A-O, and B-O of the $NiFe_2O_4$ lattice, as shown in Table 1. AN opposite result was observed in the Dx and δ values. Moreover, the peak height at the (2 2 0) and (4 4 0) reflection planes can be monitored for the cation distribution on the tetrahedral and octahedral sites that are involved in the spinel structure. The intensity ratio (I_{220}/I_{440}) of the previous planes increases as the egg white increases. This observation confirms the redistribution of the cation between the A- and B- sites when increasing the egg white content.

Table 1. Lattice parameters of $NiFe_2O_4$ nanoparticles.

Parameters	S1	S2
d, nm	4	18
a, nm	0.8284	0.8322
V, nm^3	0.5685	0.5764
D_x, g/cm^3	5.4769	5.4019
L_A, nm	0.3587	0.3603
L_B, nm	0.2928	0.2941
A-O, nm	0.1894	0.1902
B-O, nm	0.2137	0.2147
r_A, nm	0.0574	0.0582
r_B, nm	0.0817	0.0827
I_{220}/I_{440}	1.878	7.645
δ, $Lines/nm^2$	0.0625	0.0031

3.2. FTIR Analysis

Most scientists have referred to the appearance of two characteristic vibrational modes in the FTIR spectra of ferrite-based nanoparticles, depending upon the cation distribution in two different interstitial sites [3,14–17,22,27–29]. These sites are known as the A- and/or tetrahedral site and the B- and/or octahedral site. Nearly at 600 cm^{-1}, where the higher wave number, ν_1, band is found, the metal-oxygen (M-O) bond stretching vibrations at the tetrahedral site may be responsible for this band. On the other hand, the lower wave number range, ν_2, can be seen at a distance of about 400 cm^{-1}. The M-O bond vibrations in the octahedral site might be responsible for the emergence of this band. The differing values of the M-O bond lengths in the corresponding sites are what cause the different placements of these bands for the tetrahedral and octahedral complexes [17]. In other words, the value of ν_1 is generally greater than that of ν_2 because the M_{tetra}-O bond is shorter than the M_{octa}-O bond. Figure 2 displays the FTIR analysis of the S1 and S2 samples. This figure shows the ν_1 and ν_2 frequencies at 623 cm^{-1} and 500 cm^{-1} for the S1 sample and at 577 cm^{-1} and 420 cm^{-1} for the S2 sample, respectively. It is clear to us that there is a large shift in the position of bands toward the lower frequencies, from 623 cm^{-1} to 500 cm^{-1} for ν_1 and from 577 cm^{-1} to 420 cm^{-1} to for ν_2. This shift could be attributed to the solid-state reaction between both the Ni and Fe oxides, yielding Ni ferrite. However, the presence of these bands confirms the formation of $NiFe_2O_4$-based materials.
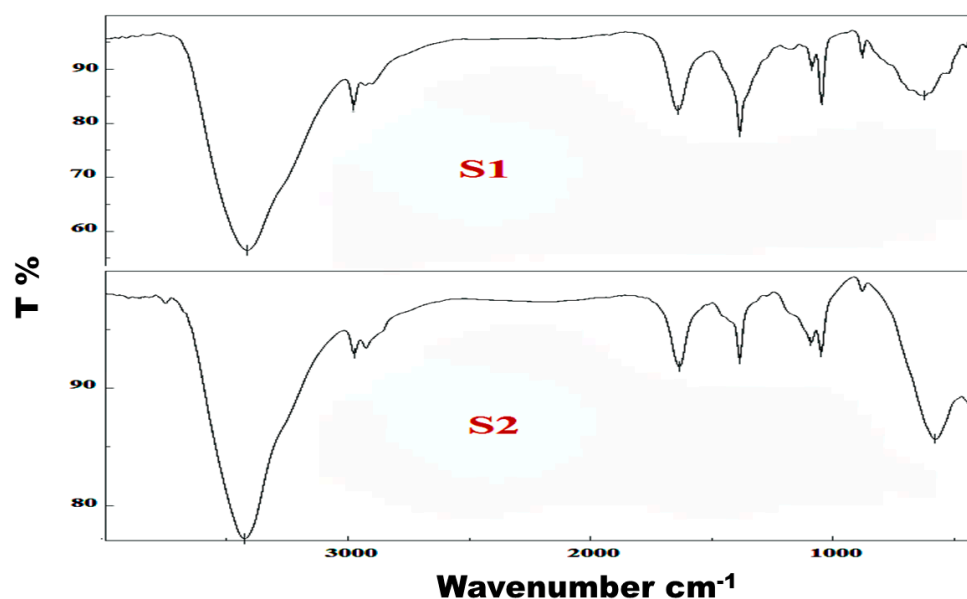
Figure 2. Fourier-transform infrared (FTIR) spectrum of S1 and S2 samples.

Furthermore, the bands at 3426–3415 cm^{-1} and 1640–1634 cm^{-1} are the stretching and bending vibrations of the hydroxyl groups (O-H) for the adsorbed water molecules on the samples' surfaces, depending upon the blending of these specimens with KBr [28]. Whereas, the bands located at 1383, 1087, and 1047 cm^{-1} could be attributed to the stretching vibrations of a hydroxyl carbon (C-O-H), depending upon the presence of carbon trace, which resulted from the autocombustion process of the egg white [28].

3.3. TEM Morphological Study

As shown in Figure 3a,b at various magnifications, TEM analysis was utilized to demonstrate the morphological properties of the S2 sample. This sample's TEM pictures revealed that the intended material contains semispherical and random nanoparticles of various sizes. The particle size was determined to be between 7 and 18 nm. Additionally, Figure 3c,d show the continuous selected-area electron diffraction (SAED) and high-resolution transmission electron microscopy (HRTEM) techniques, respectively. This figure can be used to investigate the crystallinity of the created nanoparticles. Based on the fast Fourier transform (FFT) image, as shown in Figure 3c, the metallic lattice fringe was found at 0.205 nm, which is related to the crystal plane of (311), indicating the successful synthesis of cubic spinel nickel ferrite. On the other hand, the SAED analysis shows small bright spots as rings around a central spot having different diameters. This result confirms the successful synthesis of polycrystalline nickel ferrite solid.
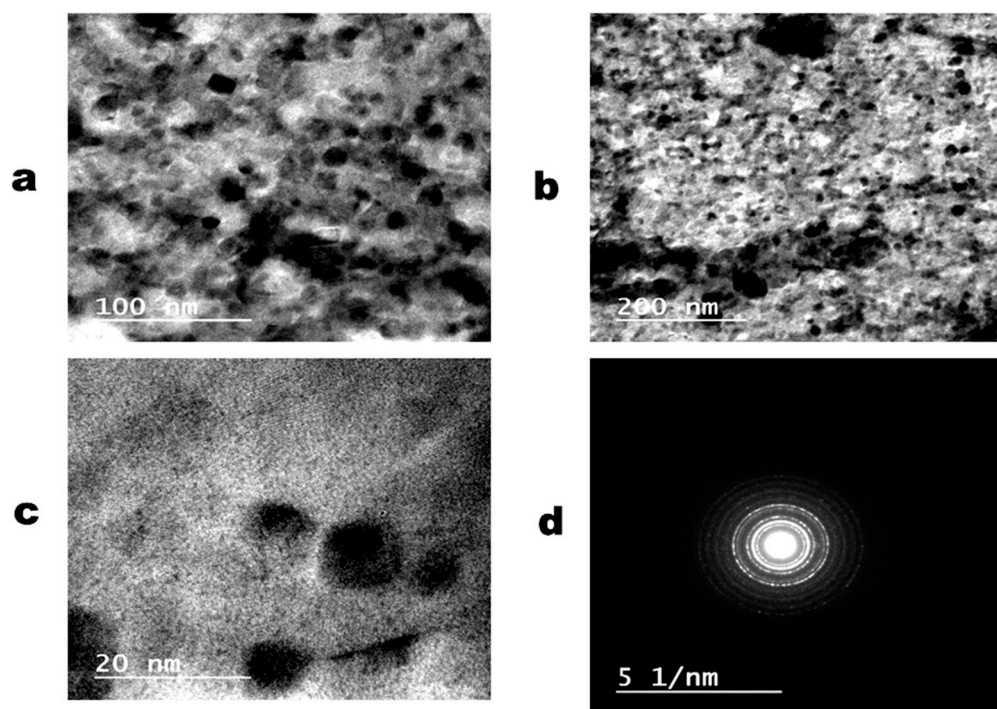
Figure 3. (**a**,**b**) various magnifications, and (**c**,**d**) selected-area electron diffraction transmission electron micrograph (TEM) images of S2 samples.

3.4. Surface Characteristics

The surface properties of the S1 and S2 samples, namely S_{BET}, V_P, V_m, and $\hat{r}$, were determined by using N_2-adsorption/desorption isotherms at 77 K. Figure 4 consists of two isotherms related to the as-prepared systems.
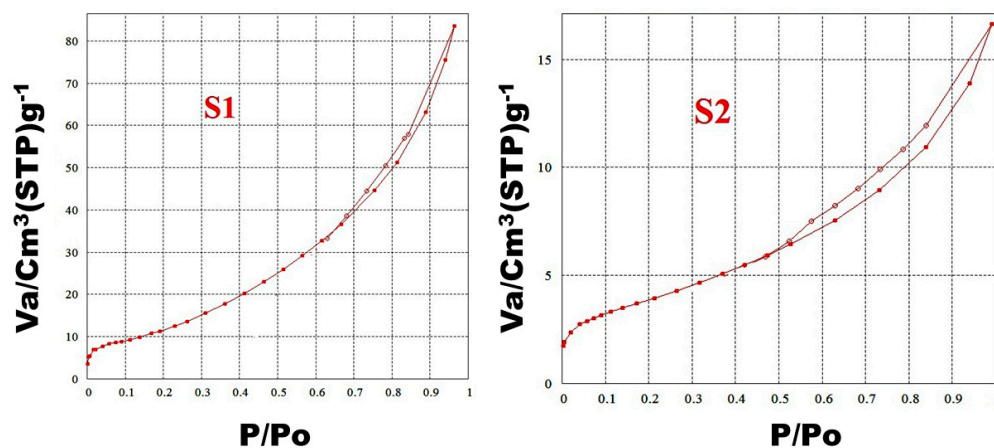
Figure 4. N_2-adsorption/desorption isotherms of S1 and S2 samples.

These isotherms, in fact, have a type H3 hysteresis loop and type II isotherms. Table 2 provides a list of the values for S_{BET}, V_p, V_m, and $\hat{r}$. This table shows that an increase in egg white content led to a marked decrease in the values of S_{BET}, V_P, V_m, and $\hat{r}$ in the S2 sample. In fact, a smaller mean pore radius may have contributed to a lower surface area value with a higher egg white percentage. On the other hand, Figure 5 shows how the distribution of pore sizes was represented.

Table 2. Surface properties of the S1 and S2 samples.

Samples	S_{BET} (m^2/g)	V_m (nm)	$\hat{r}$ (nm)	V_p (cm^3/g)	C-Constant
S1	57.258	13.183	9.0176	0.1165	13.247
S2	13.934	3.202	7.3398	0.0216	114.260
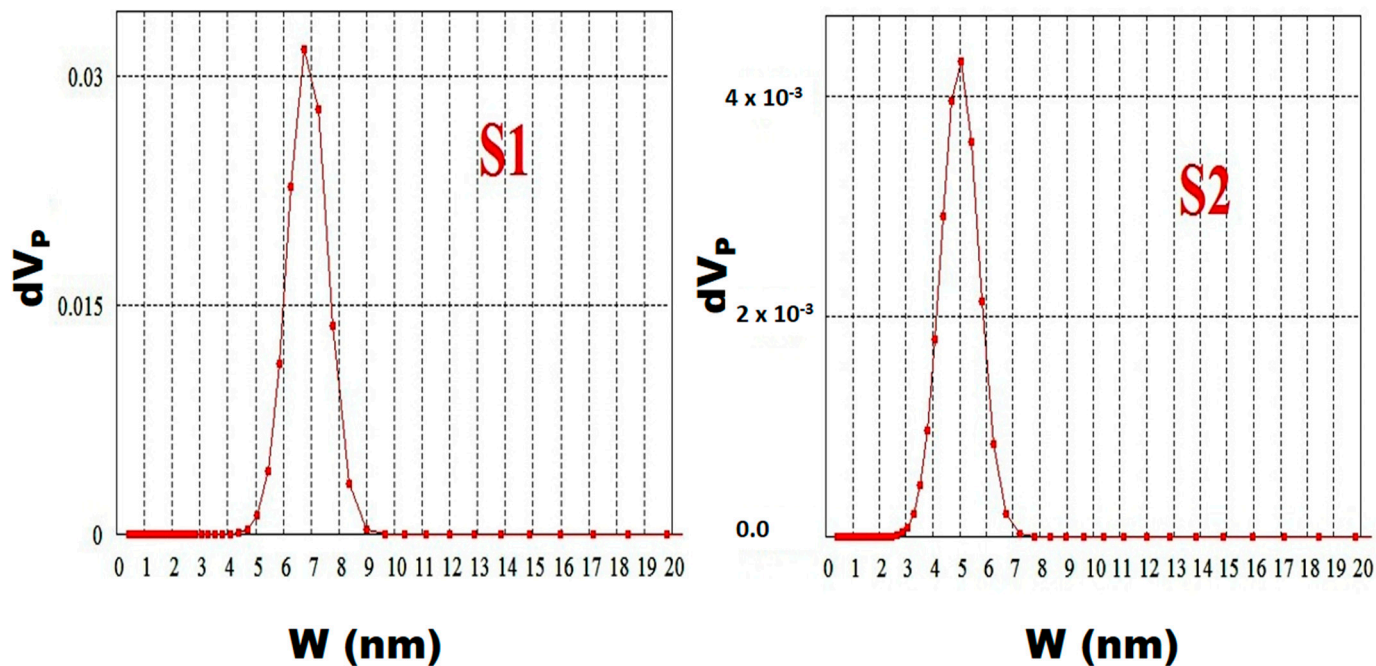
Figure 5. Pore-size distribution of S1 and S2 samples.

Most of the pores for the S1 sample have a size located in the range of 4.5–9 nm. As can be seen, the average pore size for the S1 sample is 6.75 nm. Whereas, the majority of pores for the S2 sample have a size presented in the range of 3–7.5 nm, with an average pore size of 5 nm.

3.5. Magnetic Properties

In Figure 6, the magnetization curves of the as-prepared samples are illustrated. The creation of these curves requires the use of VSM at room temperature to measure the magnetization of the synthesized materials, as a function of the applied magnetic field in the range of $-20,000$ to $+20,000$ G. The values of the synthesized solids' coercive field (H_c), remanent magnetization (M_r), saturation magnetization (M_s), squareness (M_r/M_s), anisotropy constant (K_a), initial permeability (μ_i), and magnetic moment (μ_m) per unit formula in Bohr magnetron are reported in Table 3.
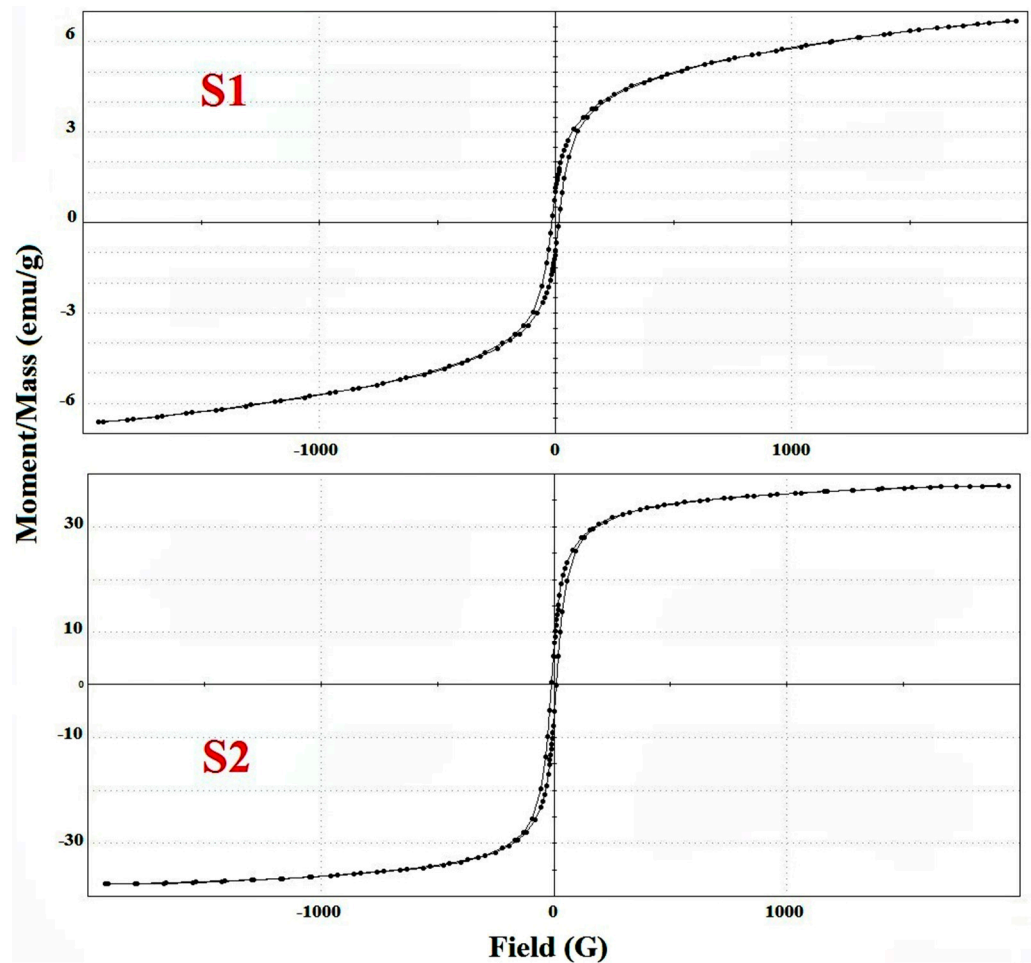
Figure 6. M–H curves at room temperature for S1 and S2 samples.

Table 3. The magnetic properties of the S1 and S2 samples.

Sample	M_s (emu/g)	μ_i	μ_m	H_c (G)	M_r/M_s (emu/g)	M_r (emu/g)	Anisotropy Constant (K_a)
S1	6.6589	0.1640	0.1527	159.15	0.1526	1.0165	1081.39
S2	37.727	5.8511	1.5834	113.74	0.1824	6.8801	4378.64

Table 3 shows that the values of M_r, M_s, M_r/M_s, μ_m, and K_a for the S2 sample are greater than those of S1 sample. In other words, an increase in egg white content brought about an increase in the values of M_r, M_s, M_r/M_s, μm, and K_a.

4. Discussion

Indeed, the contact between the surfaces of NiO and Fe_2O_3 at specified conditions resulted in the solid-state reaction between them, yielding nickel ferrite ($NiFe_2O_4$). This

reaction depends on the contact surface area between these oxides. However, this reaction can be achieved in three steps, as follows:

(i) The first step involves the formation of an initial thin layer of nickel ferrite (rigid ferrite film) surrounding these oxides, with subsequent inhibition of this reaction. In other words, this layer works as a barrier preventing the formation of excess amounts of nickel ferrite.

(ii) The second step is the diffusion of the reacting oxides and/or cations through the barrier layer, to form the excess quantities of the aforementioned ferrite. The diffusion process of the cations through the rigid ferrite film depends on the mobility of these cations. This step is the rate-determining step and/or key step of the solid–solid interaction between NiO and Fe_2O_3. There are different parameters that can be controlled in this step such as the precursors, preparation method, and doping and heat treatments [3,5,13–16].

(iii) The final step is the complete conversion of the reacting oxides to produce the studied ferrite. The following equations enabled us to shed light on the previous steps and the mechanism of the solid-state reaction between NiO and Fe_2O_3 to form $NiFe_2O_4$ [16]. At the Fe_2O_3 interface:

$$3Fe_2O_3 + Ni^{2+} \rightarrow 2NiFe_2O_4 + 2Fe^{2+} + 0.5O_2 \tag{2}$$

At the NiO interfaces:

$$2Fe^{2+} + 3NiO + 0.5O_2 \rightarrow NiFe_2O_4 + Ni^{2+} \tag{3}$$
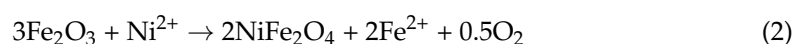
For the overall reaction:

$$3Fe_2O_3 + 3NiO \rightarrow 3NiFe_2O_4 \tag{4}$$
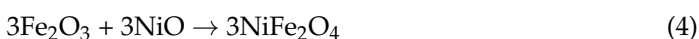
Indeed, one cannot ignore Fe_2O_3, including Fe^{2+} as a defect lattice, which can be observed at the Fe_2O_3 interface [26]. However, Fe_2O_3 decomposes to $2Fe^{2+}$ and oxygen gas at the Fe_2O_3 interface [27]. However, this speculation could be attributed to the egg-white-assisted preparation method, depending upon the reducing atmosphere for the combustion process, which reduces some or all of the metal ions through the gases released. In addition, the burning of the egg white produces a very small amount of carbon, which facilitates the reduction process of the metal ions as follows [28]:

$$2Fe_2O_3 + C \rightarrow 2FeO + CO_2 \tag{5}$$

From Equation (2), we can observe that the start of the solid-state reaction is at the Fe_2O_3 surface, forming $NiFe_2O_4$ as a rigid ferrite film with the presence of the Fe^{2+} ions and the release of oxygen. It is clear to us from Equation (3) that the Fe^{2+} ions and the released oxygen move through the rigid ferrite film to interact with the NiO to acquire more $NiFe_2O_4$ particles and Ni^{2+} ions; then, these ions diffuse again through this film to react with Fe_2O_3 to form more nickel ferrite and so on. At the end of the reaction and with the completed diffusion process, the complete transformation of the nickel and iron ions into nickel ferrites takes place, as shown by Equation (5). In other words, the counter-diffusion of the Ni^{2+} and Fe^{2+} ions with the movement of the oxygen atoms through a relatively rigid ferrite film resulted in the complete formation of the $NiFe_2O_4$ particles. This behavior shows the synergetic effect of the Fe^{2+} ions, which have a high mobility to diffuse through the rigid ferrite film and react with NiO in the presence of oxygen, yielding $NiFe_2O_4$. Finally, the formation via the diffusion of Fe^{2+} indicates the conversion of the Fe^{2+} and Fe^{3+} ions. In this study, increasing the egg white content resulted in the stimulation of the solid-state reaction between NiO and Fe_2O_3, yielding $NiFe_2O_4$ due to an increase in the realized heat, with a subsequent increase in the mobility of the reacting cations during the combustion process. This augmentation led to an increase in the crystallite size, lattice parameter, and unit cell volume of the $NiFe_2O_4$ crystallites due to the grain growth and/or agglomeration of these crystallites. The evidence that the $NiFe_2O_4$ particles have undergone grain growth

is the marked increase in the L_A, L_B, r_A, r_B, A-O and B-O values, due to the increase in the egg white content. Moreover, the increase in the value of I_{220}/I_{440} refers to an increase in the amount of the iron ions located at the tetrahedral site, indicating the stimulation of the solid-state reaction between the NiO and Fe_2O_3, yielding $NiFe_2O_4$. However, increasing the amount of egg white brought about a decrease in the dislocation of the nickel ferrite's lattice.

The FTIR measurements revealed that:

(i) The egg-white-assisted autocombustion method brought about green synthesis of $NiFe_2O_4$ nanoparticles, depending upon the presence of two main bands around 600 cm^{-1} and 400 cm^{-1}.

(ii) The as-prepared nickel ferrites have an inverse spinel structure because nickel cations have a higher preference for the octahedral site. However, the tetrahedral site completely filled with Fe^{3+} cations, and the remaining Fe^{3+} cations occupied the octahedral site.

(iii) An increase in egg white content resulted in a strong shift in the position and intensity of the two characteristic vibrational modes of nickel ferrite. This shift was observed in the case of the S2 sample toward the lower frequencies. This result confirms an increase in the crystallite size of the $NiFe_2O_4$ crystallites as the egg white increases, depending upon an increase in the lattice constant and the unit cell volume of these crystallites. This observation is consistent with the XRD results.

HRTEM and SAED analyses confirm that the as-prepared material consisted entirely of nickel ferrite-based semispherical particles with a particle size ranging between 7 nm and 18 nm. In addition, these investigations display the polycrystalline nature of the formed object. Furthermore, the FFT image for the S2 sample depicts the transformation of an image between the spatial and frequency domain. In other words, the FFT evaluates the spatial frequency distribution (i.e., feature sizes) as well as overall alignment. This image confirms that the d-spacing at 0.205 nm is attributed to the crystal plane of (311), indicating the formation of $NiFe_2O_4$.

The results of the surface properties confirm that the solid–solid interaction between the Ni and Fe oxides, yielding nickel ferrite, depends upon the strong changes in the values of S_{BET}, V_P, V_m, and $\hat{r}$, for the as-prepared solids. In general, the surface area of the individual oxides is greater than that of the product of the reaction between them. The maximum decrease in SBET, VP, and $\hat{r}$ is 75.7%, 81.5%, and 18.6%, respectively, due to an increase in the egg white content from 3 mL to 10 mL in case of the S2 sample. These observations indicate that an increase in the egg white content led to the stimulation of the solid-state reaction between the reacting oxides, producing nickel ferrite with a low surface area and a contraction in the mean pore radius, total pore volume, and pore-sized distribution. Indeed, the maximum decrease in the pore-size distribution was 25.9, indicating grain growth and/or agglomeration with an increase in the nickel ferrite content.

Investigation of the hysteresis cycle displays the effect of an applied magnetic field on the magnetization changes of the $NiFe_2O_4$ nanoparticles. The obtained hysteresis loops at room temperature show that the as-prepared nickel ferrite is typical of soft magnetic material. Room temperature ferromagnetism and/or superparamagnetism-like behaviors were observed in the as-synthesized nickel ferrites. Different factors affected the magnetic properties of the Ni ferrites such as the composition, density, surface area, defects, structure, microstructure, morphology, and cation distribution. Indeed, the cation distribution at the tetrahedral (A)/octahedral (B) sites of the spinel structure can be influenced by the ion size, crystal lattice, precursors, preparation method, composition, doping, heat treatment, stabilization energy in the crystalline field, and electronic configuration. Furthermore, the generated larger electrostatic attraction by the trivalent ion nuclei lead to their electron orbits shrinkage, with subsequent preference for the tetrahedral site [2,3,30]. On other hand, larger divalent cations prefer the octahedral site because it is bigger than the tetrahedral site [30]. In nickel ferrite, Ni^{2+} prefers the octahedral site, with subsequent migration of half the content of Fe^{3+} to the tetrahedral site, yielding an inverse spinel structure.

An increase in the M_s, μ_m, and μ_i for the S2 sample could be attributed to the augmented super-exchange interaction within the inter sublattice (A-B), which takes place between the Fe3+ ions in different sites over the oxygen ions [31]. In addition, the difference in ionic radii between Fe^{3+} (0.065 nm) and Ni^{2+} (0.069 nm) at the B sites plays an important role in determining the saturation magnetization of a ferrite [32]. On the other hand, the variation of Ms can also correlate to the higher values of the lattice parameter as well as the hopping length in the octahedral (L_A) and tetrahedral (L_B) sites. The squareness, or M_r/M_s ratio, determines the domain state that leads to the magnetization change of the studied nickel ferrite. Indeed, the synthesized ferrites fall into pseudo-single domains, depending upon the squareness being between 0.1 and 0.5 [33]. Thus, the squareness can be also linked to the magnetic anisotropy and super-exchange interaction between the cations in the tetrahedral (A) and octahedral (B) ions within the spinel lattice. These findings depend on the type and number of ions at the A and B sites [32].

5. Conclusions

The egg-white-assisted autocombustion route resulted in the formation of nanosized $NiFe_2O_4$ particles. Egg white behaves as a stabilizing/capping agent. In fact, egg white acts as a biotemplate, having advantageous features such as control over the size of nanoparticles, which reduces the agglomerations and captures the metal ion in the amylose helix in well-defined sites. A single cubic spinel-structure-based $NiFe_2O_4$ with good crystallinity and a crystallite size of about 4–18 nm was synthesized. An increase in the egg white content brought about an enhancement of the Ni ferrite formation, with an increase in the lattice parameter and the d, L_A, L_B, r_A, r_B, A-O, and B-O values of $NiFe_2O_4$. The as-prepared ferrites have a semispherical-type structure, with slight agglomerations. The surface area (S_{BET}) of the investigated solids decreases, as the egg white content increases. This decrease could be attributed to a decrease in both the total pore volume and the mean pore radius included in the porous nickel ferrites. In addition, the results of the pore-size distribution display mesoporous materials, with a pore size in the range of 3 nm to 9 nm. Finally, the magnetization of the as-synthesized material increases from 6.6589 emu/g to 37.727 emu/g, when increasing the egg white content from 3 mL to 10 mL. The opposite behavior was observed in the case of the coercivity of the studied material. The augmentation of the magnetization was discussed in terms of the augmented super-exchange interaction between the Fe^{3+} ions within the octahedral/tetrahedral sites over the oxygen ions.

Conflicts of Interest: The authors declare no conflict of interest.

References

1. Deraz, N.M. The heat treatment based soft technology for synthesis of hopcalite/hausmannite nanocomposite. *J. Ind. Environ. Chem.* **2018**, *2*, 4–6.
2. Deraz, N.M. Mechanism of oxide spinel's formation. *Sci. Fed. J. Quantum Phys.* **2018**, *2*, 1000001.
3. Alarifi, A.; Deraz, N.M.; Shaban, S. Structural, morphological and magnetic properties of $NiFe_2O_4$ nanoparticles. *J. Alloys Compd.* **2009**, *486*, 501–506. [CrossRef]
4. Valenzuela, R. Novel Applications of Ferrites. *Phys. Res. Int.* **2012**, *2012*, 591839. [CrossRef]
5. Deraz, N.M.; El-Aiashy, M.K.; Ali, S.A. Novel preparation, magneto-chemical characterization and catalytic behavior of nanocrystalline cobalt ferrite catalysts. *Adsorp. Sci. Technol.* **2009**, *27*, 803–816. [CrossRef]
6. Kumar, E.R.; Reddy, P.S.P.; Devi, G.S.; Sathiyaraj, S. Structural, dielectric and gas sensing behavior of Mn substituted spinel MFe_2O_4 (M = Zn, Cu, Ni, and Co) ferrite nanoparticles. *J. Magn. Magn. Mater.* **2016**, *398*, 281–288. [CrossRef]
7. Shan, A.; Wu, X.; Lu, J.; Chen, C.; Wang, R. Phase formations and magnetic properties of single crystal nickel ferrite ($NiFe_2O_4$) with different morphologies. *Cryst. Eng. Comm.* **2015**, *17*, 1603–1608. [CrossRef]
8. Jaffari, G.H.; Rumaiz, A.K.; Woicik, J.C.; Shah, S.I. Influence of oxygen vacancies on the electronic structure and magnetic properties of $NiFe_2O_4$ thin films. *J. Appl. Phys.* **2012**, *111*, 093906. [CrossRef]
9. Galvao, W.S.; Neto, D.M.A.; Freire, R.M.; Fechine, R.B.A. Super-paramagnetic nanoparticles with spinel structure: A review of synthesis and biomedical applications. *Solid State Phenom.* **2016**, *241*, 139–176. [CrossRef]
10. Piao, X.; Zeng, G.M.; Huang, D.L.; Feng, C.L.; Hu, S.; Zhao, M.H.; Lai, C.; Wei, Z.; Huang, G.; Xie, G.X.; et al. Use of iron oxide nanomaterials in wastewater treatment: A review. *Sci. Total Environ.* **2012**, *424*, 1–10.
11. Reddy, D.H.K.; Yun, Y.S. Spinel ferrite magnetic adsorbents: Alternative future materials for water purification. *Coord. Chem. Rev.* **2016**, *315*, 90–111. [CrossRef]
12. Hua, M.; Zhang, S.; Pan, B.; Zhang, W.; Zhang, L.L.Q. Heavy metal removal from water/wastewater by nanosized metal oxides: A review. *J. Hazard. Mater.* **2012**, *211–212*, 317–331. [CrossRef] [PubMed]
13. Deraz, N.M.; Shaban, S.A.; Alarifi, A. Removal of sulfur from commercial kerosene using nanocrystalline $NiFe_2O_4$ based sorbents. *J. Saudi Chem. Soc.* **2010**, *14*, 357–362. [CrossRef]
14. Deraz, N.M. Effects of magnesia addition on structural, morphological and magnetic properties of nanocrystalline nickel ferrite system. *Ceram. Int.* **2012**, *38*, 511–516. [CrossRef]
15. Deraz, N.M.; Abd-Elkader, O.H. Production and Characterization of Nano-Magnetic $Ni_{0.5}Zn_{0.5}Fe_2O_4$ Spinel Solid Solution. *J. Anal. Appl. Pyrolysis* **2014**, *106*, 171–176. [CrossRef]
16. Deraz, N.M.; Abd-Elkader, O.H. Processing and Characterization of Nano-Magnetic $Co_{0.5}Ni_{0.5}Fe_2O_4$ System. *J. Ind. Eng. Chem.* **2014**, *20*, 3251–3255. [CrossRef]
17. Deraz, N.M. Cation distribution: From here the beginning. *Sci. Fed. Mater. Res. Lett.* **2019**, *3*, 1000001.
18. Mohsen, Q.; Abd Elkader, O.H.; Farouk, A.; Hassan, H.M.A.; Mostafa, N.Y. Influence of tungsten substitution on structure, optical, vibrational and magnetic properties of hydrothermally prepared $NiFe_2O_4$. *Appl. Phys. A* **2021**, *127*, 296. [CrossRef]
19. Prasad, S.; Gajbhiye, N.S. Magnetic studies of nanosized nickel ferrite particles synthesized by citrate precursor technique. *J. Alloys Compd.* **1998**, *265*, 87–92. [CrossRef]
20. Chen, D.H.; He, X.R. Synthesis of nickel ferrite nanoparticles by sol–gel method. *Mater. Res. Bull.* **2001**, *36*, 1369–1377. [CrossRef]
21. Abbas, M.K.; Khan, M.A.; Mushtaq, F.; Warsi, M.F.; Sher, M.; Shakir, I.; Aly Aboud, M.F. Impact of Dy on structural, dielectric and magnetic properties of Li-Tb-nanoferrites synthesized by micro-emulsion method. *Ceram. Int.* **2017**, *43*, 5524–5533. [CrossRef]
22. Deraz, N.M. Facile and eco-friendly route for green synthesis of magnesium ferrite nano particles. *Sci. Sinter.* **2010**, *52*, 53–65. [CrossRef]
23. Al Angari, Y.M. Magnetic properties of La-substituted $NiFe_2O_4$ via egg-white precursor route. *J. Magn. Magn. Mater.* **2011**, *323*, 1835–1839. [CrossRef]
24. Wang, L.; Li, Z.; Liang, Y.; Zhao, K. Synthesis of $Ni_{0.6}Cu_{0.4}Fe_2O_4$ ferrite fine powder using egg white method. *Appl. Mech. Mater.* **2014**, *492*, 253–257. [CrossRef]
25. Maensiri, S.; Masingboon, C.; Boonchomb, B.; Seraphin, S. A simple route to synthesize nickel ferrite ($NiFe_2O_4$) nanoparticles using egg white. *Scr. Mater.* **2007**, *56*, 797–800. [CrossRef]
26. Abd-Elkader, O.; Al-Enizi, A.M.; Shaikh, S.F.; Ubaidullah, M.; Abdelkader, M.O.; Mostafa, N.Y. The Structure, Magnetic, and Gas Sensing Characteristics of W-Substituted Co-Ferrite Nanoparticles. *Crystals* **2022**, *12*, 393. [CrossRef]
27. Rehwoldt, M.C.; Wang, Y.; Xu, F.; Ghildiyal, P.; Zachariah, M.R. High-Temperature Interactions of Metal Oxides and a PVDF Binder. *ACS Appl. Mater. Interfaces* **2022**, *14*, 8938–8946. [CrossRef]
28. Al-Senani, G.M.; Al-Saeedi, S.I.; Al-Kadhi, N.S.; Abd-Elkader, O.H.; Deraz, N.M. Green Synthesis and Pinning Behavior of Fe-Doped $CuO/Cu_2O/Cu_4O_3$ Nanocomposites. *Processes* **2022**, *10*, 729. [CrossRef]
29. Vazquez-Olmos, A.R.; Abatal, M.; Sato-Berru, R.Y.; Pedraza-Basulto, G.K.; Garcia-Vazquez, V.; Sainz-Vidal, A.; Perez-Bañuelos, R.; Quiroz, A. Mechanosynthesis of MFe2O4 (M = Co, Ni, and Zn) Magnetic Nano-particles for Pb Removal from Aqueous Solution. *J. Nanomater.* **2016**, *2016*, 9182024. [CrossRef]

30. Prasad, B.V.; Ramesh, K.V.; Srinivas, A. Structural and magnetic properties of nanocrystalline nickel ferrite (NiFe$_2$O$_4$) synthesized in sol-gel and combustion routes. *Solid State Sci.* **2018**, *86*, 86–97. [CrossRef]

31. Narang, S.B.; Pubby, K. Nickel spinel ferrites: A review. *J. Magn. Magn. Mater.* **2021**, *519*, 167163. [CrossRef]

32. Wahba, A.M.; Mohamed, M.B. Structural and magnetic characterization and cation distribution of nanocrystallineCo$_x$Fe$_{3-x}$O$_4$ ferrites. *J. Magn. Magn. Mater.* **2015**, *378*, 246–252. [CrossRef]

33. Sedrati, C.; Alleg, S.; Boussafel, H.; Hacine, A.B. Structure and magnetic properties of nickel ferrites synthesized by a facile co-precipitation method: Effect of the Fe/Ni ratio. *J. Mater. Sci. Mater. Electron.* **2021**, *32*, 24548–24559.